Biosensors and Bioelectronics 246 (2024) 115918

Contents lists available at ScienceDirect

Biosensors and Bioelectronics

journal homepage: www.elsevier.com/locate/bios

Enhancing the sensitivity and stability of electrochemical aptamer-based sensors by AuNPs@MXene nanocomposite for continuous monitoring of biomarkers

Haowei Duan [a], Shi-Yang Tang [b], Keisuke Goda [c,d,e], Ming Li [a,f,*]

[a] School of Engineering, Faculty of Science and Engineering, Macquarie University, Sydney, NSW, 2109, Australia
[b] School of Electronics and Computer Science, University of Southampton, Southampton, SO16 1BJ, UK
[c] Department of Chemistry, University of Tokyo, Tokyo, 113-0033, Japan
[d] Department of Bioengineering, University of California, Los Angeles, CA, 90095, USA
[e] Institute of Technological Sciences, Wuhan University, Hubei, 430072, China
[f] School of Mechanical and Manufacturing Engineering, University of New South Wales, Sydney, NSW, 2052, Australia

ARTICLE INFO

Keywords:
Electrochemical aptamer-based sensor
MXene Ti_3C_2
Real-time monitoring
Vascular endothelial growth factor
Continuous measurement

ABSTRACT

Electrochemical aptamer-based (E-AB) sensors offer exciting potential for real-time tracking of various biomarkers, such as proteins and small molecules, due to their exceptional selectivity and adaptability. However, most E-AB sensors rely on planar gold structures, which inherently limit their sensitivity and operational stability for continuous monitoring of biomarkers. Although gold nanostructures have recently enhanced E-AB sensor performance, no studies have explored the combination of gold nanostructure with other types of nanomaterials for continuous molecular monitoring. To fill this gap, we employed gold nanoparticles and MXene Ti_3C_2 (AuNPs@MXene), a versatile nanocomposite, in designing an E-AB sensor targeted at vascular endothelial growth factor (VEGF), a crucial human signaling protein. Remarkably, the AuNPs@MXene nanocomposite achieved over thirty-fold and half-fold increases in active surface area compared to bare and AuNPs-modified gold electrodes, respectively, significantly elevating the analytical capabilities of E-AB sensors during continuous operation. After a systematic optimization and characterization process, the newly developed E-AB sensor, powered by AuNPs@MXene nanocomposite, demonstrated both enhanced stability and heightened sensitivity. Overall, our findings open new avenues for the incorporation of nanocomposites in E-AB sensor design, enabling the creation of more sensitive and durable real-time monitoring systems.

1. Introduction

Continuous measurement of biomarkers is crucial for health monitoring (García-Guzmán et al., 2021), disease diagnostics (Fan and Andrew, 2020; Guo et al., 2021; Yang et al., 2023), and precise medicine (Li and Wen, 2020; Wu et al., 2022). For example, continuous glucose monitoring devices, one of the most successful commercially available sensors, have proven to be revolutionary for diabetes management (Teymourian et al., 2020). However, these sensors monitor glucose levels in human physiological fluids based on enzymatic reactions, which cannot be applied to continuously measure other vital molecules, including proteins and nucleic acids. Although biosensors based on antigen-antibody interactions (e.g., enzyme-linked immunosorbent assays, ELISA (Engvall et al., 1971)) can operate continuously to detect different types of biomolecules, they always suffer from instable bioreceptors, high cost as well as time-consuming batch processing, limiting their practicability for frequently repeated measurements (Jarczewska and Malinowska, 2020; Ma et al., 2020).

Aptamers, short single-stranded DNA or RNA oligos that recognize and bind to a broad range of specific target analytes (e.g., proteins, cells, and small molecules) with high affinity and specificity (Ellington and Szostak, 1990; Tuerk and Gold, 1990), can address the above-mentioned limitations of biosensors. Due to their unique features (e.g., ease of modification and conjugation, low synthesis cost, and high chemical stability), aptamers have been integrated with a variety of readout methods, including electrochemistry, surface-enhanced Raman scattering (SERS), fluorescence, and colorimetry (Iliuk et al., 2011; Wu et al., 2021), for the detection of biomarkers. Among these

---

* Corresponding author. School of Mechanical and Manufacturing Engineering, University of New South Wales, Sydney, NSW, 2052, Australia.
E-mail address: ming.li3@unsw.edu.au (M. Li).

https://doi.org/10.1016/j.bios.2023.115918
Received 6 October 2023; Received in revised form 21 November 2023; Accepted 5 December 2023

ligand-specific biosensing platforms, electrochemical aptamer-based (E-AB) sensors are most popular, owing to their compact size, simple operation, and high selectivity in complex environments (e.g., body fluids) (Downs and Plaxco, 2022; Schoukroun-Barnes et al., 2016). Moreover, E-AB sensors have shown great advances in real-time, continuous and *in vivo* molecular monitoring (Ferguson et al., 2013; García-Guzmán et al., 2021).

However, conventional E-AB sensors based on planar gold electrodes remain suboptimal for continuous measurements of analytes over long time periods, due to limited sensitivity (Downs and Plaxco, 2022) and significant signal drift during repeated interrogations (Shaver and Arroyo-Currás, 2022). To enhance the analytical performance of E-AB sensors including signal gain and signal-to-noise (S/N) ratio, gold nanostructures, such as porous-(Downs et al., 2021; Fu et al., 2021), spindle-(Taheri et al., 2018), and dendritic-(Liu et al., 2014) shaped gold, have been applied in E-AB sensors, because of their high surface areas and the ability to accelerate electron transfer efficiency. In addition, hybrid nanostructures composed of gold and other types of nanomaterials, including graphene (Kong et al., 2023; Wei et al., 2018), carbon nanotube (He et al., 2019; Liu et al., 2019), metal-organic framework (Rasheed and Rizwan, 2022; Su et al., 2017; Wei et al., 2022) and MXene (Huang et al., 2022; Sinha et al., 2018; Yang et al., 2022; Zahra et al., 2022), have been used for the construction of E-AB sensors. These hybrid nanomaterials synergistically combine the intrinsic properties of the individual components, making them exhibit unique features, such as abundant surface terminal groups, high biocompatibility and intriguing electrochemical behaviors. Despite a few studies have demonstrated that the use of nanocomposite can improve the signal gain and sensitivity of E-AB sensors for single-point measurement (Chandra et al., 2011; Ni et al., 2020), it remains unclear whether such enhancement of E-AB sensors can be achieved for continuous biomarker monitoring. This is because E-AB sensors require to be interrogated more frequently for continuous measurement, which induces significant degradation of aptamer probes (Watkins et al., 2023) followed by the change of analytical sensitivity (White et al., 2008). Moreover, the impact of nanocomposite on other crucial factors of E-AB sensors (e.g., noise level and stability of electrochemical signals) (Downs et al., 2021; Watkins et al., 2023) has not been studied for continuous molecular quantification.

In this work, we develop a hybrid nanostructured E-AB sensor based on gold nanoparticles incorporated MXenes Ti_3C_2 (AuNPs@MXene) for continuous monitoring of protein, which shows much higher stability and sensitivity than E-AB sensors based on bare gold and AuNPs modified gold. MXenes Ti_3C_2, a relatively new type of two-dimensional nanomaterial, has been proven as an ideal matrix for the development of cutting-edge E-AB sensors (Huang et al., 2022; Sinha et al., 2018; Yang et al., 2022). By integrating MXene and AuNPs, the nanocomposite constructed interface significantly increased active surface area, a key factor in improving E-AB biosensing ability (Fu et al., 2021). For proof-of-concept, vascular endothelia growth factor (VEGF), a vital biomarker for the diagnostics of various diseases (e.g., cancers, neurological disorders and inflammation) (Carmeliet, 2005; Dehghani et al., 2018; Zhu et al., 2017), is selected as a model analyte. We employed a VEGF-binding aptamer previously reported in literature (Nick Taylor et al., 2008; Potty et al., 2009; Zhao et al., 2011) with high binding affinity and selectivity, which has widely been adapted for electrochemical sensing of VEGF (Amouzadeh Tabrizi et al., 2017; Feng et al., 2020). After conjugated with the AuNPs@MXene modified electrode surface, this aptamer undergoes rapid and reversible conformational changes in the presence of VEGF, thus enabling the continuous molecular quantification. Under optimal working conditions (e.g., electrochemical interrogations and aptamer probe density), our sensor exhibited an average of twice higher signal gain and a remarkably improved signal stability compared to E-AB sensors using planer gold electrodes. Moreover, our E-AB sensor empowered by AuNPs@MXene nanocomposites was challenged in artificial urine and also exhibited improved noise level, higher drift-resistance and better real-time sensitivity than the ones constructed on bare gold and AuNPs modified gold. To the best of our knowledge, this is the first time that the improvement in real-time, continuous sensing performance of E-AB sensors by nanocomposites has been reported.

2. Material and methods

2.1. Materials and reagents

Sulfuric acid, tris(2-carboxyethyl) phosphine hydrochloride (TCEP), 6-mercapto-1-hexanol (MCH), human vascular endothelial growth factor-165 (VEGF), gold (III) chloride trihydrate ($HAuCl_4{\bullet}3H_2O$), human Immunoglobulin G (IgG), human sourced albumin, creatine, human tumour necrosis factor-alpha (TNF), bovine serum albumin (BSA), sulfuric acid (H_2SO_4), sodium dodecyl sulphate (SDS), artificial urine diluent, phosphate buffered saline (PBS) were purchased from Sigma–Aldrich, Australia. MXene Ti_3C_2 (5 mg/mL) were purchased from Beike Xincai Technology, China. The buffer solutions used in this study was prepared in PBS unless otherwise stated. Ultrapure deionized water (DI, 18.2 MΩ cm) was used in all experiments. A thiol- and methylene blue (MB)- modified aptamer (5′-HS-$(CH_2)_6$-TTCCCGTCTTCCAGACAAGAGTGCAGGG-MB-3′) was used as the sensing probe and synthesized by Bioneer, Korea. This aptamer sequence was adapted from previous reports (Nick Taylor et al., 2008; Potty et al., 2009; Zhao et al., 2011), exhibiting a high affinity with a dissociation constant (K_d) about 10.9 nM and good specificity (Potty et al., 2009). Table S1 lists the sequences and functionalities of all oligos used in this study.

2.2. Fabrication of AuNPs@MXene modified gold electrodes

Screen-printed gold electrodes (SPGE, C-220AT) were purchased from Metrohm, Australia, with gold-working and counter areas, and silver as reference electrode. 5 mg/mL of MXene Ti_3C_2 flakes was diluted into different concentrations with water, followed by drop-casting on the gold working electrode (AuE) and then dried under nitrogen flow. Electrochemical deposition (Othman et al., 2022) was employed for the construction of AuNPs interface on MXene. The detailed procedure of this gold functionalization method is described in Supplementary Information. To visualize the surface morphologies of the resultant interfaces, scanning electron microscopy (SEM) images were collected at 15 kV by JSM-7100 instrument (JEOL, Japan).

2.3. Fabrication of AuNPs@MXene-empowered E-AB sensor

The thiolated aptamers were reduced by 1000 times concentrated TCEP solution for 2 h at room temperature (~23 °C). 10 μL of aptamer solutions with different concentrations (50 nM–5 μM) were applied on the surface of freshly prepared electrodes, followed by overnight incubation at 4 °C in a humanity chamber. After thoroughly rinsing with DI water, the electrodes were immersed in 30 mM MCH water solution to remove non-specifically or loosely bonded probes, forming a well-packed self-assembled monolayer of aptamers. Afterward, the electrodes were rinsed thoroughly with DI water again, and then dried with nitrogen flow prior to electrochemical tests.

2.4. Determination of active surface area

Cyclic voltammetry (CV) measurement was employed to determine the active surface area of the gold electrodes as described previously (Trasatti and Petrii, 1991). Briefly, we applied potentials from −0.5 to 1.2 V on the electrodes immersed in 0.5 M H_2SO_4 to absorb oxygen. Integration of the area under the reduction current is equal to the charge (in coulombs) associated with the reduction of gold oxide layer. Finally, this value of charge was divided by a factor of 400 μC per cm^2 to obtain the electroactive area of gold electrode in units of cm^2 (Trasatti and

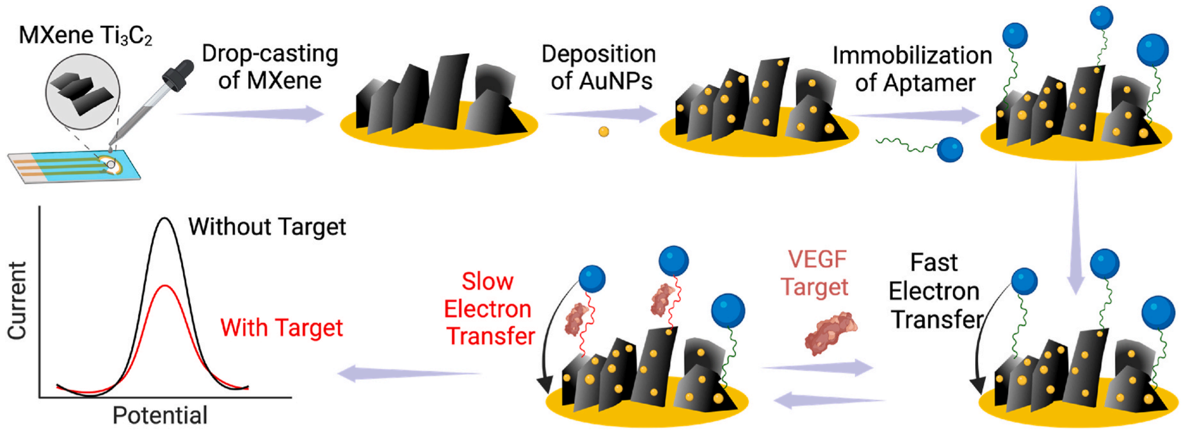

Fig. 1. Schematic illustration of the AuNPs@MXene-empowered E-AB sensor for VEGF detection.

Petrii, 1991). The peak area under this reduction current was calculated for active surface determination in Nova (version 2.1, Metrohm).

2.5. Detection of VEGF by AuNPs@MXene-empowered E-AB sensor

All electrochemical tests were carried out using SPGE in a three-electrode system, consisting of gold as counter and working electrodes, and silver (Ag) as reference electrode. The target induced signal changes on our sensor were analyzed using alternating current voltammetry (ACV) and square wave voltammetry (SWV) with a potential amplitude of 25 mV, and a potential range from −0.1 to −0.5 V (vs. Ag). To evaluate the impact of frequency on signal changes, frequency ranges from 25 to 200 Hz and 25–350 Hz were applied for ACV and SWV experiments, respectively. The density of aptamer probes on the electrode surface was determined using ACV as described elsewhere (Sumner et al., 2000). The peak current in ACV quantifies electron transfer from MB and the amount of immobilized aptamer probes on electrode surface (Lao et al., 2005). Chronoamperometric interrogation of our sensor was conducted at potentials serially stepped from −0.1 to −0.5 V with a duration of 100 ms for each step and an interval time of 10 μs. To evaluate target binding induced changes in electrochemical characteristics, a VEGF solution at a saturation concentration of 130 nM was used, and the signal at a saturation point was collected after 1 h of incubation.

3. Results and discussion

3.1. Fabrication and mechanism of AuNPs@MXene-empowered E-AB sensor

Fig. 1 illustrates the fabrication process and sensing mechanism of

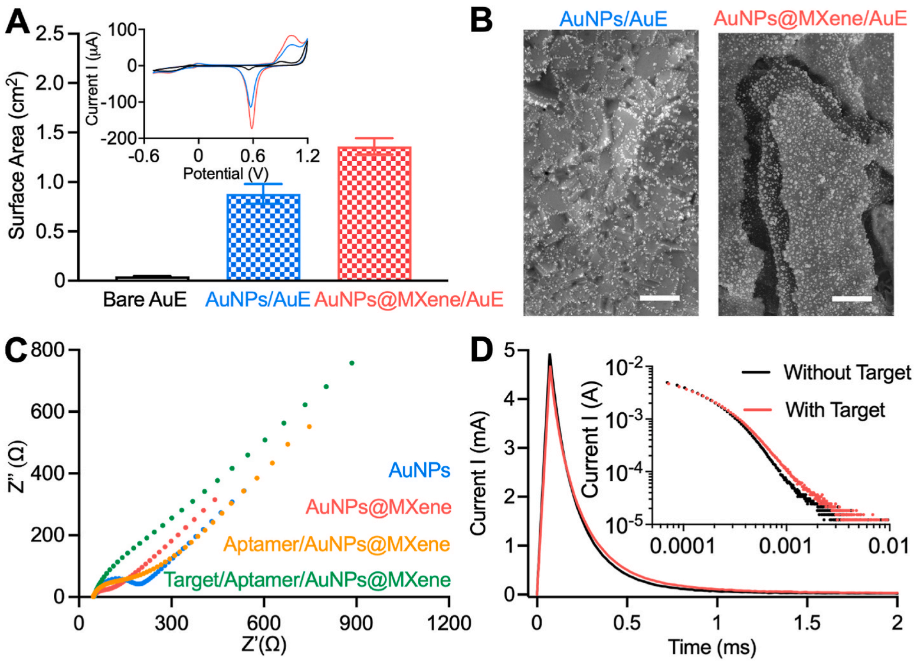

Fig. 2. Characterization of AuNPs@MXene nanocomposite and its empowered E-AB sensor. **(A)** Comparison of electroactive surface areas of three types of electrodes, bare gold electrode (bare AuE, black), AuNPs/AuE (blue) and AuNPs@MXene/AuE modified (red) electrodes. Inset is the representative CV curves measured using three types of electrodes. **(B)** SEM images of AuNPs/AuE (left), AuNPs@MXene/AuE (right) prepared by electrochemical deposition. Scale bar, 1 μm. **(C)** Representative EIS results of AuNPs (blue), AuNPs@MXene (red), Aptamer/AuNPs@MXene (yellow) and Target/Aptamer/AuNPs@MXene (green) based interfaces. EIS were performed in 10 mM PBS solution containing 5 mM $[Fe(CN)_6]^{3-/4-}$. **(D)** Chronoamperometry plots of AuNPs@MXene-empowered E-AB sensor before (black) and after (red) binding of target VEGF. Chronoamperometry measurements were performed with step potentials from 0 V to −0.4 V, which cover the formal potential of methylene blue redox reaction.

the AuNPs@MXene-empowered E-AB sensor for real-time monitoring of VEGF, a signal protein regulates angiogenesis and vasculogenesis activities in human. MXene solution was firstly drop-casted on the working electrode, which was followed by electrochemical deposition of AuNPs in the presence of $HAuCl_4$. Then, VEGF aptamers were immobilized on the surface of AuNPs@MXene nanocomposite modified AuE (AuNPs@MXene/AuE) via gold-thiol interaction between thiolated aptamer probe and decorated gold nanoparticles. ACV and SWV were used to quantify electron transfer between aptamer conjugated methylene blue (MB) and electrode surface. In the absence of target, aptamers in their unbound state exhibit more effective electron transfer, as evidenced by a relatively high peak current in the voltammetry plot (black line). Upon target binding, surface-tethered aptamers undergo conformational change, altering the spatial position of the MB redox molecule away from the electrode surface. Thus, the specific binding between target VEGF and aptamers generates a reduction in relative current (red line) that is proportional to the concentrations of VEGF.

3.2. *Validation of AuNPs@MXene-empowered E-AB sensor*

The active surface area of E-AB sensors is a key factor affecting their sensing performance, including sensitivity, limit of detection and signal to noise ratio. The microscopic surface of gold is proportional to the integrated area under the CV curves of the constructed electrodes, which is corresponding to the reduction of the gold oxide monolayer during CV scanning. After comparing the resultant interfaces constructed using three different methods, including dropcasting (Duan et al., 2023), electrochemical roughening (Arroyo-Currás et al., 2017), and electrochemical deposition, we selected the electrochemical deposition method (see Supporting Information Section S1) to prepare gold nanoparticles decorated MXene, due to its reproducibility and simplicity (data not shown).

The active surface area of AuNPs@MXene/AuE was compared to the ones of two other types of electrodes: bare gold electrode (bare AuE) and AuNPs modified gold electrode (AuNPs/AuE). As shown in Fig. 2A, the maximum surface area was obtained from the AuNPs@MXene/AuE, which exhibits ~ half- and ~thirty-fold increases in area compared to AuNPs/AuE and bare AuE, respectively. This demonstrates the role of MXene Ti_3C_2 in enhancing the active surface area of E-AB sensors.

Next, SEM images of different electrodes were obtained to visualize the changes in electrode surface morphology during stepwise electrochemical deposition. Compared to AuNPs modified AuE (Fig. 2B left), deposition of AuNPs on the MXene modified gold showed a higher density of AuNPs distribution (see Fig. 2B right). Especially, two-dimensional MXene with interlayer structures provides increased surface area for AuNPs deposition, which can be also observed from other areas of AuNPs@MXene/AuE (Fig. S4A&S4B) and remained stable over long-term storage (Fig. S4C&S4D). The differences in active gold area between AuNPs/AuE and AuNPs@MXene/AuE revealed by SEM images agreed with the ones calculated based on CV curves (Fig. 2A, inset).

Using electrochemical impedance spectroscopy (EIS) and cyclic voltammetry (CV), we evaluated the impedimetric properties, as well as charge- and electron-transfer processes of AuNPs alone and AuNPs@MXene nanocomposite modified AuEs. This gives us a better understanding of the roles of MXene in the synthesized nanocomposite. Nyquist plots were fitted by a Randles equivalent circuit, where semicircle diameter represents charge transfer resistance (R_{ct}) (Xu et al., 2019), as shown in Fig. 2C. Compared to AuNPs only group ($R_{ct} = 197\ \Omega$, blue), AuNPs@MXene nanocomposite improved interfacial charge transfer by ~8.2 times ($R_{ct} = 24\ \Omega$, red). This is because MXene has excellent electrochemical properties and enables the accumulation of more AuNPs than bare AuE, as confirmed by SEM images. After passivated by self-assembled monolayers (SAMs) of aptamer and MCH, a higher R_{ct} value (140 Ω, yellow) was obtained, due to the repelling

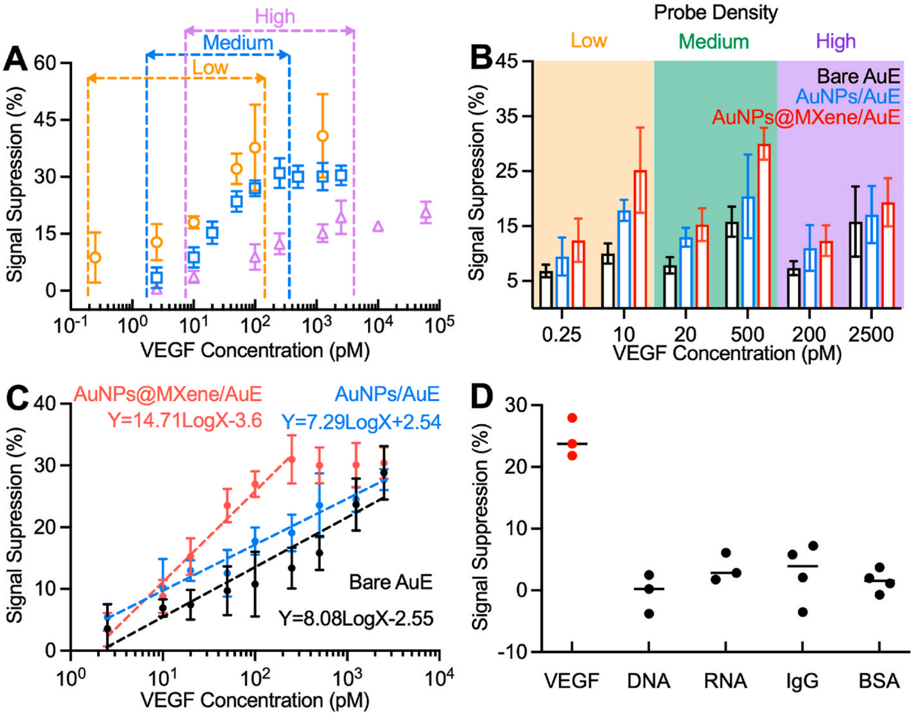

Fig. 3. Performance of AuNPs@MXene-empowered E-AB sensor for VEGF detection. **(A)** Logarithmic plot of signal suppression versus VEGF concentration for AuNPs@MXene-empowered E-AB sensors with varied aptamer coverage. **(B)** Comparison of signal suppression of E-AB sensors using bare AuE (black), AuNPs/AuE (blue) and AuNPs@MXene/AuE (red) for the detection of VEGF. **(C)** Comparison of signal suppression of E-AB sensors with a moderate probe coverage in the presence of target VEGF at different concentrations. For bare AuE (black), AuNPs/AuE (blue) and AuNPs@MXene/AuE (red) based E-AB sensors, R squared of the fitting lines are 0.78, 0.84 and 0.92, respectively. **(D)** Detection of 100 pM of target VEGF, two non-target nucleic acids (DNA and RNA) and two non-target proteins (human immunoglobulin G, IgG, and bovine serum albumin BSA) with AuNPs@MXene-empowered E-AB sensor. Interferents were applied at a concentration of 100 nM. The error bars represent the standard deviations of replicates obtained from at least three independently fabricated sensors.

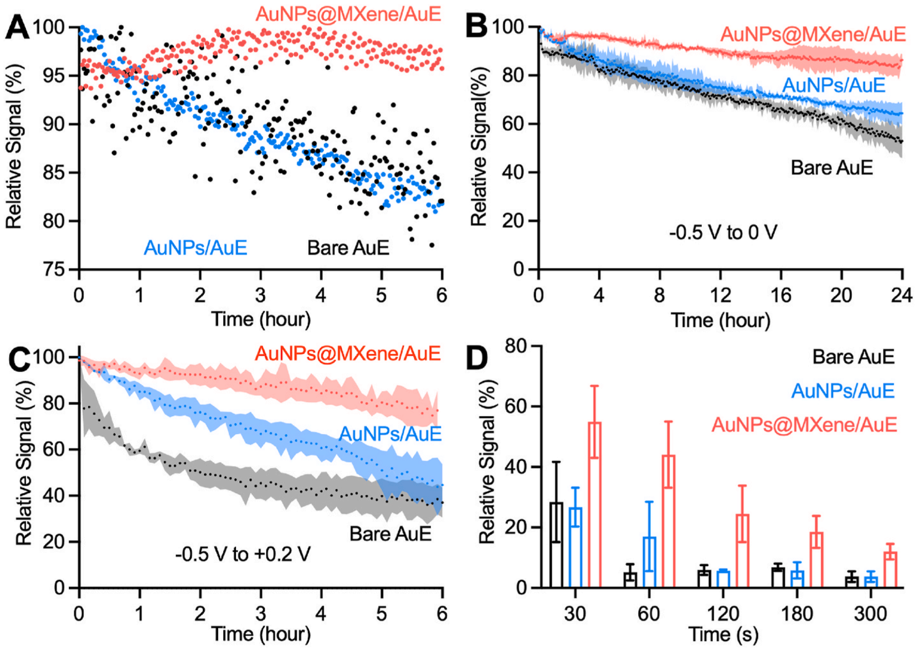

Fig. 4. AuNPs@MXene-empowered E-AB sensors achieve higher signal to noise levels and signal stability than E-AB sensors employing bare gold and AuNPs only modified bare gold. **(A)** Comparison of signal to noise levels of E-AB sensors using bare AuE (black), AuNPs/AuE (blue) and AuNPs@MXene/AuE (red). **(B)** Relative signal variations obtained on E-AB sensors using bare AuE (black), AuNPs/AuE (blue) and AuNPs@MXene/AuE (red) during continuous ACV interrogations in a time course of 24 h. Initial signals were collected after they reach relative steady status. **(C)** Comparison of relative signal retention on E-AB sensors using bare AuE (black), AuNPs/AuE (blue) and AuNPs@MXene/AuE (red) under positive potential limits extended from −0 V to +0.2 V. The colour-shaded regions reflect standard deviation of replicates using at least three independently fabricated sensors. **(D)** Comparison of relative signal retention on E-AB sensors using bare AuE (black), AuNPs/AuE (blue) and AuNPs@MXene/AuE (red) over time when applying a constant potential at −0.7 V. Error bars represent standard deviation of replicates using three independently fabricated sensors.

effects of SAM on negatively charged ferri- and ferrocyanide complex (Magar et al., 2021; Xu et al., 2019). The value of R_{ct} further increased to 235 Ω, with the presence of target VEGF (green).

Of note, the target-mediated change in EIS was collected after overnight incubation, because we were not able to observe a significant variation in interfacial interactions within a short incubation period. Similar to EIS study, CV plots (see Fig. S5) of the AuNPs/AuE shows a well-defined reversible current peak due to the redox reaction of $[Fe(CN)_6]^{3-/4-}$ species, exhibiting a peak-to-peak separation of 87 mV. The increased magnitude of peak current with a relatively smaller peak-to-peak separation (i.e., 78 mV) upon the addition of MXene suggests the enhanced electron transfer efficiency (Elgrishi et al., 2018). These observations verified the effects of two-dimensional MXene with interlayer spacing on enhancing the electrical conductivity and accelerating charge/electron mobilities, which are important for improving the analytical performance of E-AB sensors.

To evaluate the effects of target binding on the electron transfer kinetics, we further performed chronoamperometry, a more sensitive and faster voltage-controlled method. The chronoamperometric current-time responses measured before (black) and after (red) VEGF binding represented the altered electron transfer from MB moiety to the AuNPs@MXene/AuE (see Fig. 2D). Since the current transients from I-t curves were originated from the redox process of the aptamer-tethered MB, both cases can be fitted in two-exponential phases as expected for a surface-confined reaction (Arroyo-Currás et al., 2018; Santos-Cancel et al., 2018). In the presence of target, there was a slower decay in current transient, which suggested an inhibited electron transfer on the aptamer in its target-bound state. Such target-modulated differences in current between bound (with target) and unbound (without target) states can be better illustrated in a log-log plot (Fig. 2D, inset).

3.3. *Optimization of sensing conditions*

To obtain the best sensing performance of AuNPs@MXene-empowered E-AB sensor, a serial of critical parameters, including SDS pretreatment, interrogation methods and frequency, and incubation time were optimized, as described in the Supplementary Information. It is worth noting that the E-AB sensors used in this study were pretreated with a 10% SDS solution to obtain more uniform probe orientation (Wu et al., 2019). The 10% SDS pretreatment altered the polarity and magnitude of target-induced signals (Figs. S6 and S7) and, more importantly, enabled the improvement in the reproducibility and sensitivity of our sensor. Moreover, ACV interrogation at a frequency of 50 Hz was selected for future experiments, as it yielded the maximum signal change (see Fig. S8). As shown in Fig. S9, the response rate of our sensor in the presence of target VEGF is rapid, as 50% of the maximum signal suppression was achieved within 10 min after adding 2.5 nM VEGF. In the presence of target, the sensor equilibrates within 40 min, thus an incubation time of 40 min was selected for sensitivity studies.

3.4. *Detection performance of AuNPs@MXene-empowered E-AB sensor*

Utilizing the optimal SDS pretreatment and interrogation conditions, we evaluated the effect of aptamer probe density on signal gain (current suppression). The density of aptamer probes is a well-recognized key factor influencing the performance of E-AB sensors, such as limit of detection (LOD) and detection range. By varying the concentrations of VEGF aptamers, we successfully controlled the number of aptamers immobilized on the electrode surface, which was calculated by ACV measurements (Lao et al., 2005)(see Fig. S10 and Table S2). The probe density was selected at three different concentration ranges, $0.632–6.517 \times 10^{10}$, $0.711–7.381 \times 10^{11}$ and $0.494–4.816 \times 10^{12}$ (molecules per cm^2) for low, medium and high surface coverage, respectively. For AuNPs@MXene-empowered E-AB sensors, both the magnitude of the signal suppression and the range of detectable concentrations of target VEGF changed with aptamer surface coverage (see Fig. 3A). Specifically, E-AB sensors with a lower aptamer probe coverage are more sensitive for lowly abundant VEGF (with concentrations ranging from 100 fM to 100 pM), and exhibited an excellent limit of detection of 16 fM according to signal-to-noise (S/N) ratio of 3. With the increase of probe density, both detection range and LOD of E-AB sensors shifted towards higher concentrations, due to the combined effects of probe repellence and aptamer affinity (White et al., 2008).

Moreover, AuNPs@MXene-empowered sensors were compared to E-AB sensors using bare AuE and AuNPs/AuE, both of which were functionalized with similar aptamer coverages for VEGF detection (see Fig. 3B). For E-AB sensors based on bare gold, no clear enhancement in signal suppression was observed at different probe coverages, which is likely because of the relatively low affinity of aptamer probes on planer gold electrode. AuNPs/AuE-based and AuNPs@MXene-empowered E-AB sensor, in contrast, improved the signal change in the presence of target VEGF at the same concentrations. Remarkably, AuNPs@MXene-empowered E-AB sensors exhibited the highest signal changes among three groups, which is attributed to the improvement in electrochemical properties (i.e., electron transfer rate) and surface areas with the assistance of MXene. The moderate aptamer coverage was chosen for future experiments, considering a tradeoff between sensitivity and clinically relevant levels of VEGF.

We also compared the signal changes on bare AuE, AuNPs/AuE and AuNPs@MXene-empowered E-AB sensors, in the presence of target VEGF at different concentrations ranging from 2.5 to 2500 pM. As shown in Fig. 3C, a larger amount of signal suppression was obtained on our sensor than E-AB sensors using bare gold and AuNPs/AuE. Moreover, a linear relationship between signal suppression and VEGF concentrations ranging from 2.5 to 250 pM was obtained. Due to similar amount of immobilized aptamer probes, the signal suppression levels, saturating at around 30%, are comparable across E-AB sensors based on different electrodes, whereas we observed earlier signal saturation on the AuNPs@MXene interface. The steeper slope of the response curve for the developed sensor, compared to those based on bare AuE and AuNPs/AuE, demonstrated its superior sensitivity in VEGF detection. This is possible ascribed to the enhanced accessibility of aptamer probe (Mahshid et al., 2017; Soleymani et al., 2009) and the accelerated electron transfer (Fu et al., 2021) on the AuNPs@MXene nanostructured electrode. This distinction underscores the essential role of the AuNPs@MXene nanocomposite in promoting the sensitivity of E-AB sensors. In addition, the binding-induced signal of our sensor is highly selective against interferents, including nucleic acids (DNA and RNA fragments) and proteins (human immunoglobulin G, IgG, and bovine serum albumin, BSA) at a concentration (i.e., 100 nM) that is 1000 times as high as the concentration of target VEGF (see Fig. 3D).

3.5. Signal stability of AuNPs@MXene-empowered E-AB sensor

We further assessed the noise level and signal stability of AuNPs@MXene-empowered E-AB sensors, as they are major and decisive parameters that impact long-term operations. As shown in Fig. 4A, AuNPs@MXene-empowered E-AB sensor produced a low baseline noise level (with a standard deviation of ~1.51 %). In contrast, E-AB sensor fabricated on a planar AuE provided relatively high noise signals (i.e., with a standard deviation of ~4.95 %), while AuNPs/AuE-based E-AB sensor exhibited relatively rapid signal degradation, making them less suitable for accurate and continuous measurements. In addition to the decrease in the noise level of baseline, AuNPs@MXene also enhanced signal retention on E-AB interface, which is crucially important for continuous operations. As shown in Fig. 4B, both bare AuE, AuNPs/AuE and AuNPs@MXene-empowered E-AB sensors exhibited linear trends of signal degradation under continuous ACV scans, presumably due to electrochemistry-driven desorption of thiolated aptamers and oxidation of the gold surface (Leung et al., 2021; Zhong and Porter, 1997). However, our developed AuNPs@MXene-empowered E-AB sensor exhibited a much slower degradation rate than bare AuE- and AuNPs/AuE-based E-AB sensors. After 24-h interrogation, bare AuE- and AuNPs/AuE-based, and AuNPs@MXene-empowered E-AB sensors experienced average signal losses of 47%, 36% and 17%, respectively. In addition, the developed sensor also exhibited higher signal retention over two weeks of storage compared to their AuNPs/AuE counterpart (see Fig. S11). Such enhancement in signal stability on the AuNPs@MXene-empowered E-AB sensor is likely originated from synergistic effects of more stable electrochemical property, stronger thiol-gold interaction, and robust surface morphology (see Fig. S4).

To verify our hypotheses, we firstly evaluated the stability of electrochemical property on different surface constructs by performing CV in PBS solution containing $[Fe(CN)_6]^{3-/4-}$. During continuous CV scans, current intensity of anodic redox peak reflects the rate of electron transfer between $[Fe(CN)_6]^{3-/4-}$ and electrode interface, which can be used to quantify the degradation of electrode surfaces (Chan et al., 2022). Over 400 consecutive CV scans (see Fig. S13), AuNPs@MXene modified electrode retained largest relative anodic current compared to ones from bare AuE and AuNPs/AuE, demonstrating the higher robustness and stability of the nanocomposite-constructed interface. Then, we investigated the signal degradation on bare AuE-, AuNPs/AuE-based and AuNPs@MXene-empowered E-AB sensors under the influence of potential. According to previous reports (Leung et al., 2021), the desorption rate of aptamer monolayers is strongly dependent on the potential window used to interrogate E-AB sensors. As the positive potential limit extended from 0 V to +0.2 V (Fig. 4C), dramatically exacerbated degradations of relative signals were observed on the E-AB sensors using bare AuE (black) and AuNPs/AuE (blue). This is mainly because of the stronger oxidation of Au substrate under the increased limit of positive potential (Leung et al., 2021). In comparison, AuNPs@MXene-empowered E-AB sensors (red) are less susceptible to this process, as indicated by a maximum 25% signal loss over 6-h scanning compared to the 64% and 55% signal loss over the same period on bare AuE- and AuNPs/AuE-based E-AB sensors, respectively.

In addition, we applied a negative enough potential (i.e., −0.7 V) and monitored signal losses over time on E-AB sensors (Sen and Lazenby, 2023). Under this negative potential, the desorption and removal of thiolated aptamer monolayer from gold substrate is triggered, thus allowing us to quantify the stability and strength of gold-thiol bond on E-AB sensors constructed using different electrodes. Due to the potential-derived breakage of thiol-gold bond, bare AuE and AuNPs/AuE lost almost all relative signal within 60 s, while our developed sensor based on AuNPs@MXene/AuE retained an average of 44% of initial signal in the same period. We found out that around 12% of signal was retained on AuNPs@MXene/AuE even after 300-s desorption. These observations demonstrated that our developed sensor has a higher resistance to the degradation of gold and thiol-gold interactions, revealing possible mechanisms behind the improvement in signal stability of E-AB sensors empowered by AuNPs@MXene nanocomposite. Of note, the signal stability of our sensor achieved under a wider potential window is important for implementing versatile strategies to E-AB sensors. For example, it has been reported that degradation rate of E-AB signal can be mitigated by narrowing the applied potential window (Leung et al., 2021; McHenry et al., 2022). However, changing potential window encounters difficulties in selection of the accurate potential range for voltammetric measurements, as the potential range for the redox reaction is shifted under repetitive measurements (McHenry et al., 2022). In addition, much wider potential range should be used to simultaneously detect multiple targets (Grabowska et al., 2022) or perform dual-reporter drift correction (Li et al., 2016) on E-AB biosensors. This will accelerate the breakage of thiol-gold bond and the degradation rate of E-AB signal. In this regard, our developed sensor could avoid the above mentioned issues.

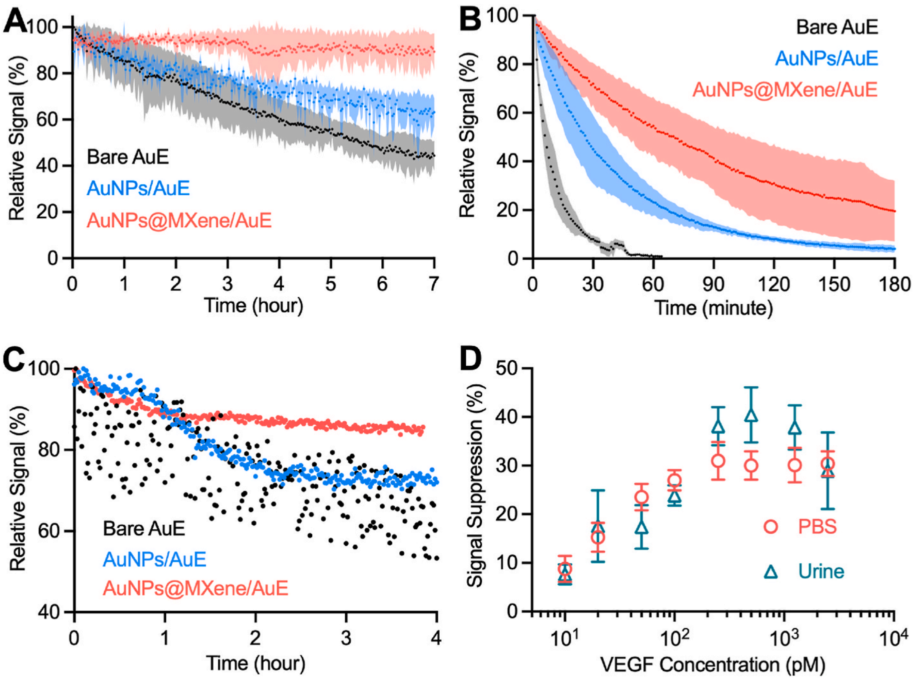

Fig. 5. Stability and performance of our sensor with the ferrocene containing probe and in artificial urine. Comparison of the signal stability of **(A)** MB-containing DNA monolayers in urine solution and **(B)** Ferrocene-containing DNA monolayers on bare AuE (black), AuNPs/AuE (blue) and AuNPs@MXene/AuE (red). (**C**) Improved baseline noise level of the AuNPs@MXene modified interface when interrogated in urine. (**D**) Comparison of the performance of the developed sensor for VEGF detection in PBS buffer and urine solution. The color-shaded regions and error bars reflect standard deviation of replicates from three electrodes that were fabricated independently.

3.6. Compatibility of the improved stability for AuNPs@MXene-empowered E-AB sensor

We further assessed whether the enhancement in the stability of E-AB sensors enabled by AuNPs@MXene nanocomposite can be observed under different electrolyte and redox species conditions. VEGF level in urine is a crucial predictor of chronic kidney-related disease (CKD) and plays an important role in diagnosing and regulating CKD (Avguštin et al., 2017; Chan et al., 2004). As shown in Fig. 5A, after replacing PBS with urinary electrolyte, the signal degradation became more rapid for both bare gold and MXene modified interfaces, presumably due to more ionic species present in urine solution. Nevertheless, AuNPs@MXene-empowered E-AB sensor delivered higher signal retention than bare AuE-based E-AB sensors over the same time course of interrogation. To better understand the role of MXene in the improvement of signal retention, we also performed the same tests with AuNPs modified E-AB sensors. Similarly, E-AB sensors modified by AuNPs@MXene nanocomposite (AuNPs@MXene/AuE) exhibited a higher signal retention than the ones without MXene modification (i.e., AuNPs/AuE), thus revealing the importance of MXene in improving signal stability.

The degradation rate of a ferrocene (Fc) redox reporter, with a different redox potential (i.e., +0.23 V) compared to MB (i.e., −0.25 V), was also assessed on different electrode constructs. The characterization of Fc probes requires a different voltammetry potential window (from 0 V to + 0.5 V) to MB, over which the thiol-gold bond becomes instable and thus reduces the stability of the attached probes (Kang et al., 2009, 2016). As shown in Fig. 5B, continuous scanning of Fc-containing DNA monolayers exhibited a much rapid decrease in relative signals compared to MB-containing DNA monolayers, which agrees with the findings in previous studies (González-Fernández et al., 2016; Kang et al., 2009). Specifically, Fc signal disappeared completely after 60- and 180- min voltammetric scan, respectively, on bare AuE and AuNPs/AuE. AuNPs@MXene-empowered E-AB sensor, in contrast, delivered a much slower degradation speed and retained more than 20% relative signals of Fc reporters over 180 min. The enhancement of signal longevity on both MB and Fc conjugated SAM suggests the modification strategy using AuNPs@MXene nanocomposite is generalizable, and will be beneficial for the construction of E-AB sensors with different types of redox reporters. Of note, MXene has lower catholic stability than graphene and its derivates (Zahra et al., 2022), so we anticipate that more stable signals for the gold-tethered reporters with positive redox potentials can be obtained when incorporating AuNPs with cathodically stable materials.

Moreover, the developed AuNPs@MXene-empowered E-AB sensor also exhibited a much better baseline noise level than E-AB sensors constructed on bare AuE and AuNPs/AuE in urine matrix (see Fig. 5C). AuNPs@MXene modification significantly reduced baseline noise and signal drift, thus enabling more accurate target detection in complex environment (e.g., undiluted blood sample and living body). We next compared the performance of our sensor for detecting VEGF in urinary and buffered solutions. As shown in Fig. 5D, in comparison with samples analyzed in PBS, similar values of signal suppression were obtained when employing our sensor directly in urinary solution, suggesting that our sensor remains robust for VEGF detection under varied buffer conditions. Of note, the saturated signal in urine matrix reached at slightly higher plateaus compared to ones in PBS solution, probably due to the accelerated current drift in urine as previously observed.

3.7. Real-time monitoring of VEGF

To verify whether the improved sensitivity and stability enabled by AuNPs@MXene are applicable for continuous operations in complex environment, we deployed our sensor for tracking VEGF dynamics in artificial urine. Despite that ACV raw data can be used to quantify VEGF concentration based on the degradation rate of relative current (see Fig. S14), other factors (e.g., electrode fouling by proteins, aptamer degradation driven by nuclease) can accelerate the degradation rate of the signal. Thus, it is challenge to establish a reliable baseline, which hinders the use of ACV raw data to quantify the concentrations of targets accurately and in real time.

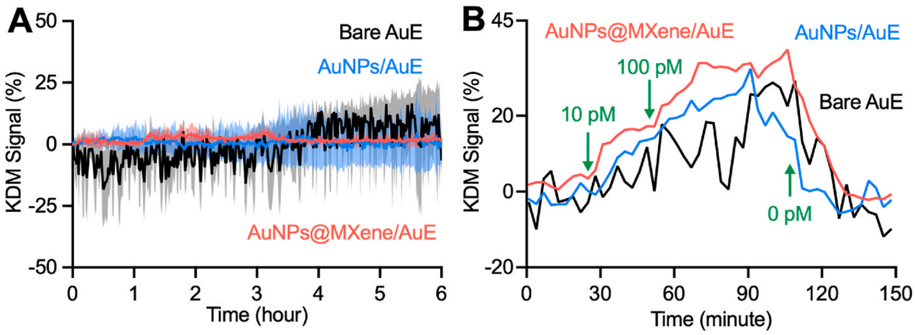

Fig. 6. Real-time monitoring of VEGF at clinically relevant threshold levels in artificial urine using AuNPs@MXene-empowered E-AB sensor. **(A)** AuNPs@MXene/AuE based E-AB sensor (red) shows much lower levels of noise and signal variation than E-AB sensors based on bare AuE (black) and AuNPs/AuE (blue). **(B)** Using KDM correction, our sensor (red) could detect VEGF at clinically relevant levels (green arrows) more accurately compared to the E-AB sensor based on bare AuE (black) and AuNPs/AuE (blue).

Therefore, we implemented a ratiometric strategy, namely kinetic differential measurement (KDM), to interpret target dynamics more accurately and easily (Ferguson et al., 2013). Briefly, KDM leverages the strong frequency dependence of E-AB sensors and corrects signal drift by taking the difference between two faradaic current values under high- and low-frequency voltammetric experiments. We chose SWV (see Fig. S15) for KDM experiments, as its interrogation can be completed within a much shorter time period than ACV, thus allowing a rapid signal acquisition at a higher frequency. A drift-free baseline (see Fig. S15) was obtained on AuNPs@MXene-empowered E-AB sensor after KDM correction. Also, we compared the KDM signal stability of our sensor with the E-AB sensor constructed on the bare AuE and AuNPs/AuE. As shown in Fig. 6A, the KDM signal collected from AuNPs@MXene-empowered E-AB sensor maintained higher stability and less noise level over 6 h of interrogation, with less than 1.6% of signal variation. The KDM baselines for bare AuE- and AuNPs/AuE-based E-AB sensors, in contrast, underwent significant shift with more than 6.5% and 11% of signal variation, respectively.

To demonstrate the real-time sensing performance of our sensor, we deployed it to detect the variations in the concentration of VEGF within clinically meaningful range in urine solution. After establishing a stable KDM baseline, our sensor responded rapidly and reversibly to different concentrations of target VEGF (see Fig. 6B and Fig. S16A). In comparison with E-AB sensors using bare AuE and AuNPs/AuE, the AuNPs@MXene-empowered E-AB sensor yields an improved S/N and larger KDM change (Fig. S16B), which is crucially important for accurate monitoring of lowly abundant targets. Such improvement is because AuNPs@MXene nanocomposite has demonstrated to improve the sensitivity for single point measurement (Fig. 3B and C), noise level (Fig. 4A and 5C) and signal stability (Fig. 4B and 5 A) during continuous interrogations. To verify the sensitivity, stability, and specificity of the developed sensor, we further evaluated the performance of our sensor for real-time detection of target VEGF in the presence of common urinary biomarkers (i.e., creatinine, human sourced-albumin, immunoglobulin G, and tumour necrosis factor-alpha). When challenged in artificial urine with these interferents, the developed sensor maintained high stability and a low noise level, like the one in interferent-free urine (Fig. S17A). Moreover, our sensor achieved similar signal changes against target VEGF (Fig. S17B), while no detectable response observed upon the addition of interferents. These results indicated the specificity and usefulness of the developed sensor for detecting VEGF in more complex biofluids.

4. Conclusion

In summary, we developed a AuNPs@MXene nanocomposite empowered electrochemical aptamer-based (E-AB) sensor for more sensitive and stable detection of VEGF in a continuous manner. The incorporation of MXene with AuNPs significantly improved the surface area and electrochemical properties of the E-AB interface, thus enhancing the sensitivity, limit of detection, and signal stability of the developed sensor. During high-frequency and continuous interrogations, the AuNPs@MXene modification was found to enable remarkable signal robustness and noise level for E-AB sensors, regardless of the buffer condition and reporter type. This suggest that our strategy based on the use of AuNPs@MXene nanocomposite is generalizable for constructing E-AB sensors with prolonged working duration. Overall, our approach provides valuable insights into the development of nanocomposite functionalized E-AB sensors for biomarker detection.

CRediT authorship contribution statement

Haowei Duan: Conceptualization, Data curation, Formal analysis, Investigation, Methodology, Validation, Visualization, Writing – original draft, Writing – review & editing. **Shi-Yang Tang:** Funding acquisition, Writing – review & editing. **Keisuke Goda:** Funding acquisition, Writing – review & editing. **Ming Li:** Conceptualization, Methodology, Resources, Writing – original draft, Writing – review & editing, Visualization, Supervision, Project administration, Funding acquisition.

Declaration of competing interest

The authors declare that they have no known competing financial interests or personal relationships that could have appeared to influence the work reported in this paper.

Data availability

Data will be made available on request.

Acknowledgments

This research is supported mainly by the Australian Research Council (ARC) Discovery Project (DP200102269) and partly by JSPS Core-to-Core Program. Ming Li was supported by National Health and Medical Research Council (NHMRC) Emerging Leadership Fellowship (GNT2017679). Haowei Duan acknowledges the financial support from iMQRES scholarship at Macquarie University. The authors also thank Dr. Chao Shen and Dr. Sue Lindsay at the Microscopy Unit of Macquarie University for their assistance with FE-SEM imaging. Fig. 1 is created with BioRender.com.

Appendix A. Supplementary data

Supplementary data to this article can be found online at https://doi.org/10.1016/j.bios.2023.115918.

References

Amouzadeh Tabrizi, M., Shamsipur, M., Saber, R., Sarkar, S., 2017. Sensor. Actuator. B Chem. 240, 1174–1181.

Arroyo-Currás, N., Dauphin-Ducharme, P., Ortega, G., Ploense, K.L., Kippin, T.E., Plaxco, K.W., 2018. ACS Sens. 3 (2), 360–366.

Arroyo-Currás, N., Scida, K., Ploense, K.L., Kippin, T.E., Plaxco, K.W., 2017. Anal. Chem. 89 (22), 12185–12191.

Avguštin, N., Rotar, Ž., Pajek, J., Kovač, D., Osredkar, J., Lindič, J., 2017. Clin. Nephrol. 88 (13), 10–13.

Carmeliet, P., 2005. Oncology 69 (Suppl. 3), 4–10. Suppl. 3.

Chan, D., Chien, J.-C., Axpe, E., Blankemeier, L., Baker, S.W., Swaminathan, S., Piunova, V.A., Zubarev, D.Y., Maikawa, C.L., Grosskopf, A.K., Mann, J.L., Soh, H.T., Appel, E.A., 2022. Adv. Mater. 34 (24), 2109764.

Chan, L.W., Moses, M.A., Goley, E., Sproull, M., Muanza, T., Coleman, C.N., Figg, W.D., Albert, P.S., Ménard, C., Camphausen, K., 2004. J. Clin. Oncol. 22 (3), 499–506.

Chandra, P., Noh, H.-B., Won, M.-S., Shim, Y.-B., 2011. Biosens. Bioelectron. 26 (11), 4442–4449.

Dehghani, S., Nosrati, R., Yousefi, M., Nezami, A., Soltani, F., Taghdisi, S.M., Abnous, K., Alibolandi, M., Ramezani, M., 2018. Biosens. Bioelectron. 110, 23–37.

Downs, A.M., Gerson, J., Hossain, M.N., Ploense, K., Pham, M., Kraatz, H.-B., Kippin, T., Plaxco, K.W., 2021. ACS Sens. 6 (6), 2299–2306.

Downs, A.M., Plaxco, K.W., 2022. ACS Sens. 7 (10), 2823–2832.

Duan, H., Wang, Y., Tang, S.-Y., Xiao, T.-H., Goda, K., Li, M., 2023. Sensor. Actuator. B Chem. 380, 133342.

Elgrishi, N., Rountree, K.J., McCarthy, B.D., Rountree, E.S., Eisenhart, T.T., Dempsey, J. L., 2018. J. Chem. Educ. 95 (2), 197–206.

Ellington, A.D., Szostak, J.W., 1990. Nature 346 (6287), 818–822.

Engvall, E., Jonsson, K., Perlmann, P., 1971. Biochim. Biophys. Acta Protein Struct. 251 (3), 427–434.

Fan, R., Andrew, T.L., 2020. J. Electrochem. Soc. 167 (3), 037542.

Feng, Y., Xiao, S., Xiong, X., Wang, H., Kong, F., Li, Y., Zhang, Y., Chen, L., 2020. Electroanalysis 32 (8), 1843–1849.

Ferguson, B.S., Hoggarth, D.A., Maliniak, D., Ploense, K., White, R.J., Woodward, N., Hsieh, K., Bonham, A.J., Eisenstein, M., Kippin, T.E., Plaxco, K.W., Soh, H.T., 2013. Sci. Transl. Med. 5 (213), 213ra165-213ra165.

Fu, K., Seo, J.-W., Kesler, V., Maganzini, N., Wilson, B.D., Eisenstein, M., Murmann, B., Soh, H.T., 2021. Adv. Sci. 8 (23), 2102495.

García-Guzmán, J.J., Pérez-Ràfols, C., Cuartero, M., Crespo, G.A., 2021. TrAC, Trends Anal. Chem. 135, 116148.

González-Fernández, E., Avlonitis, N., Murray, A.F., Mount, A.R., Bradley, M., 2016. Biosens. Bioelectron. 84, 82–88.

Grabowska, I., Hepel, M., Kurzątkowska-Adaszyńska, K., 2022. Advances in design strategies of multiplex electrochemical aptasensors. Sensors 22 (1), 161.

Guo, Y., Liu, X., Peng, S., Jiang, X., Xu, K., Chen, C., Wang, Z., Dai, C., Chen, W., 2021. Comput. Biol. Med. 129, 104163.

He, B., Wang, L., Dong, X., Yan, X., Li, M., Yan, S., Yan, D., 2019. Food Chem. 300, 125179.

Huang, Y., Pei, X., Du, S., Li, Z., Gu, X., Sun, W., Niu, X., 2022. Microchem. J. 181, 107774.

Iliuk, A.B., Hu, L., Tao, W.A., 2011. Anal. Chem. 83 (12), 4440–4452.

Jarczewska, M., Malinowska, E., 2020. Anal. Methods 12 (25), 3183–3199.

Kang, D., Ricci, F., White, R.J., Plaxco, K.W., 2016. Anal. Chem. 88 (21), 10452–10458.

Kang, D., Zuo, X., Yang, R., Xia, F., Plaxco, K.W., White, R.J., 2009. Anal. Chem. 81 (21), 9109–9113.

Kong, F., Luo, J., Jing, L., Wang, Y., Shen, H., Yu, R., Sun, S., Xing, Y., Ming, T., Liu, M., Jin, H., Cai, X., 2023. Nanomaterials 13 (7).

Lao, R., Song, S., Wu, H., Wang, L., Zhang, Z., He, L., Fan, C., 2005. Anal. Chem. 77 (19), 6475–6480.

Leung, K.K., Downs, A.M., Ortega, G., Kurnik, M., Plaxco, K.W., 2021. ACS Sens. 6 (9), 3340–3347.

Li, G., Wen, D., 2020. J. Mater. Chem. B 8 (16), 3423–3436.

Li, H., Arroyo-Currás, N., Kang, D., Ricci, F., Plaxco, K.W., 2016. J. Am. Chem. Soc. 138 (49), 15809–15812.

Liu, J., Wagan, S., Dávila Morris, M., Taylor, J., White, R.J., 2014. Anal. Chem. 86 (22), 11417–11424.

Liu, X., Deng, K., Wang, H., Li, C., Zhang, S., Huang, H., 2019. Microchim. Acta 186 (6), 347.

Ma, H., Ó'Fágáin, C., O'Kennedy, R., 2020. Biochimie 177, 213–225.

Magar, H.S., Hassan, R.Y.A., Mulchandani, A., 2021. Sensors 21 (19).

Mahshid, S.S., Vallée-Bélisle, A., Kelley, S.O., 2017. Anal. Chem. 89 (18), 9751–9757.

McHenry, A., Friedel, M., Heikenfeld, J., 2022. Biosensors 12 (10).

Ni, S., Shen, Z., Zhang, P., Liu, G., 2020. Anal. Chim. Acta 1121, 74–82.

Nick Taylor, J., Darugar, Q., Kourentzi, K., Willson, R.C., Landes, C.F., 2008. Biochem. Biophys. Res. Commun. 373 (2), 213–218.

Othman, A., Bilan, H.K., Katz, E., Smutok, O., 2022. Chemelectrochem 9 (9), e202200099.

Potty, A.S.R., Kourentzi, K., Fang, H., Jackson, G.W., Zhang, X., Legge, G.B., Willson, R. C., 2009. Biopolymers 91 (2), 145–156.

Rasheed, T., Rizwan, K., 2022. Biosens. Bioelectron. 199, 113867.

Santos-Cancel, M., Lazenby, R.A., White, R.J., 2018. ACS Sens. 3 (6), 1203–1209.

Schoukroun-Barnes, L.R., Macazo, F.C., Gutierrez, B., Lottermoser, J., Liu, J., White, R.J., 2016. Annu. Rev. Anal. Chem. 9 (1), 163–181.

Sen, D., Lazenby, R.A., 2023. Anal. Chem. 95 (17), 6828–6835.

Shaver, A., Arroyo-Currás, N., 2022. Curr. Opin. Electrochem. 32, 100902.

Sinha, A., Dhanjai, Zhao, H., Huang, Y., Lu, X., Chen, J., Jain, R., 2018. TrAC, Trends Anal. Chem. 105, 424–435.

Soleymani, L., Fang, Z., Sargent, E.H., Kelley, S.O., 2009. Nat. Nanotechnol. 4 (12), 844–848.

Su, F., Zhang, S., Ji, H., Zhao, H., Tian, J.-Y., Liu, C.-S., Zhang, Z., Fang, S., Zhu, X., Du, M., 2017. ACS Sens. 2 (7), 998–1005.

Sumner, J., Weber, K., Hockett, L.A., Creager, S., 2000. J. Phys. Chem. B 104.

Taheri, R.A., Eskandari, K., Negahdary, M., 2018. Microchem. J. 143, 243–251.

Teymourian, H., Barfidokht, A., Wang, J., 2020. Chem. Soc. Rev. 49 (21), 7671–7709.

Trasatti, S., Petrii, O., 1991. Pure Appl. Chem. 63 (5), 711–734.

Tuerk, C., Gold, L., 1990. Science 249 (4968), 505–510.

Watkins, Z., Karajic, A., Young, T., White, R., Heikenfeld, J., 2023. ACS Sens. 8 (3), 1119–1131.

Wei, B., Mao, K., Liu, N., Zhang, M., Yang, Z., 2018. Biosens. Bioelectron. 121, 41–46.

Wei, P., Wang, S., Wang, W., Niu, Z., Rodas-Gonzalez, A., Li, K., Li, L., Yang, Q., 2022. Appl. Surf. Sci. 604, 154369.

White, R.J., Phares, N., Lubin, A.A., Xiao, Y., Plaxco, K.W., 2008. Langmuir 24 (18), 10513–10518.

Wu, L., Wang, Y., Xu, X., Liu, Y., Lin, B., Zhang, M., Zhang, J., Wan, S., Yang, C., Tan, W., 2021. Chem. Rev. 121 (19), 12035–12105.

Wu, Y., Midinov, B., White, R.J., 2019. ACS Sens. 4 (2), 498–503.

Wu, Y., Tehrani, F., Teymourian, H., Mack, J., Shaver, A., Reynoso, M., Kavner, J., Huang, N., Furmidge, A., Duvvuri, A., Nie, Y., Laffel, L.M., Doyle III, F.J., Patti, M.-E., Dassau, E., Wang, J., Arroyo-Currás, N., 2022. Anal. Chem. 94 (23), 8335–8345.

Xu, X., Makaraviciute, A., Kumar, S., Wen, C., Sjödin, M., Abdurakhmanov, E., Danielson, U.H., Nyholm, L., Zhang, Z., 2019. Anal. Chem. 91 (22), 14697–14704.

Yang, D.S., Ghaffari, R., Rogers, J.A., 2023. Science 379 (6634), 760–761.

Yang, J., Zhong, W., Yu, Q., Zou, J., Gao, Y., Liu, S., Zhang, S., Wang, X., Lu, L., 2022. Molecules 27 (6).

Zahra, Q.u.A., Ullah, S., Shahzad, F., Qiu, B., Fang, X., Ammar, A., Luo, Z., Abbas Zaidi, S., 2022. Prog. Mater. Sci. 129, 100967.

Zhao, S., Yang, W., Lai, R.Y., 2011. Biosens. Bioelectron. 26 (5), 2442–2447.

Zhong, C.-J., Porter, M.D., 1997. J. Electroanal. Chem. 425 (1), 147–153.

Zhu, X., Kou, F., Xu, H., Lin, L., Yang, G., Lin, Z., 2017. Sensor. Actuator. B Chem. 253, 660–665.